Recovery of Heavy Metal Ions Using Magnetic Glycine-Modified Chitosan-Application to Aqueous Solutions and Tailing Leachate

Asmaa Benettayeb, Amine Morsli, Khalid Z Elwakeel, Mohammed F Hamza, Eric Guibal

applied sciences

MDPI

Article

Recovery of Heavy Metal Ions Using Magnetic Glycine-Modified Chitosan—Application to Aqueous Solutions and Tailing Leachate

Asmaa Benettayeb [1,*], Amine Morsli [1,2], Khalid Z. Elwakeel [3,4], Mohammed F. Hamza [5,6] and Eric Guibal [7,*]

1 Laboratoire de Génie Chimique et de Catalyse Hétérogène, Université de Sciences et de la Technologie—Mohamed Boudiaf, BP 1505 El-M'Nouer, Oran 31000, Algeria; morsli_amine@yahoo.fr
2 Laboratoire d'Ingénierie des procédés de l'Environnement (LIPE)—Université des Sciences et Technologie d'Oran—Mohamed Boudiaf, BP 1505 El-M'Nouer, Oran 31000, Algeria
3 Department of Chemistry, College of Science, University of Jeddah, Jeddah 80327, Saudi Arabia; kelwkeel@uj.edu.sa
4 Environmental Science Department, Faculty of Science, Port-Said University, Port Said 42522, Egypt
5 Guangxi Key Laboratory of Processing for Non-Ferrous Metals and Featured Materials, School of Resources, Environment and Materials, Guangxi University, Nanning 530004, China; m_fouda21@hotmail.com
6 Nuclear Materials Authority, El-Maadi, Cairo P.O. Box 530, Egypt
7 Polymers Composites and Hybrids (PCH), IMT Mines Ales, F-30319 Alès, France
* Correspondence: asma.benettayeb@gmail.com (A.B.); eric.guibal@mines-ales.fr (E.G.)

Featured Application: Metal removal from contaminated water bodies and metal recovery from industrial effluents (valorization).

check for updates

Citation: Benettayeb, A.; Morsli, A.; Elwakeel, K.Z.; Hamza, M.F.; Guibal, E. Recovery of Heavy Metal Ions Using Magnetic Glycine-Modified Chitosan—Application to Aqueous Solutions and Tailing Leachate. *Appl. Sci.* **2021**, *11*, 8377. https://doi.org/10.3390/app11188377

Academic Editor: Jaecheul Yu

Received: 28 June 2021
Accepted: 6 September 2021
Published: 9 September 2021

Publisher's Note: MDPI stays neutral with regard to jurisdictional claims in published maps and institutional affiliations.

Abstract: The necessity of decontaminating effluents for the dual purpose of environmental beneficiation and valorization of low-grade resources is driving the development of new sorbents. The functionalization of biopolymers is a promising strategy for improving sorption performance. Incorporating magnetic micro-particles offers an opportunity for the facilitated recovery of spent micron-size sorbent. Combining magnetic facilities and biopolymer functionalization represents a winning strategy. Magnetic glycine-grafted chitosan (G@MChs) was synthesized for the sorption of Ni(II), Zn(II), and Hg(II) before being applied to the removal of hazardous and strategic metals from tailing leachates. The sorbent was characterized using Fourier transform infrared spectroscopy and scanning electron microscopy, before and after metal sorption. The acid–base properties of functionalized sorbent were also determined (pH_{PZC}). Uptake kinetics were studied in mono- and multi-component solutions using different equations for kinetic modeling at optimized pH (i.e., pH_0: 5.5). Langmuir and Sips equations were applied to model sorption isotherms in single-component solutions. In addition, sorption isotherms in multi-component solutions were used to evaluate the preference for selected metals. Maximum sorption capacities were 0.35 mmol Hg g^{-1}, 0.47 mmol Zn g^{-1}, and 0.50 mmol Ni g^{-1}. Acidified urea solution (pH 2.7) successfully desorbs metal ions from G@MChs (desorption > 90%). The sorbent was tested for the recovery of hazardous and strategic metal ions from acidic leachates of tailings. This study demonstrates the promising performance of G@MChs for the treatment of complex metal-bearing solutions.

Keywords: magnetic glycine modified chitosan; multicomponent solution; isothermal and kinetic analysis; waste leachate

1. Introduction

The increasing demand placed on water supply due to population growth, agriculture needs, and industrial uses has led to the implementation of drastic regulations at international and national levels for the discharge of wastewater into the environment.

The accumulation of contaminants, such as heavy metals, in the food chain may explain the special attention they have received from the community and regulators. Decreasing the levels of metal ions in water bodies is not only critical for ensuring the availability of drinkable water for human and animal feed, but also for the recycling of water flows. The recovery of metals (especially strategic and valuable elements) is also strongly encouraged to optimize their use from finite resources (based on availability but also on geopolitical criteria). Therefore, the valorization of metal resources from secondary reserves (tailings, waste materials, and so on) is of critical importance, with strong political incentives for developing recycling facilities.

Depending on the water flow, metal concentration, complexity of solutions and final objective (recovery optimization vs. effluent decontamination), different methods can be used for metal recovery. Solvent extraction [1,2] is usually preferred for the recovery of valuable metals from high-concentration solutions, while precipitation techniques are more appropriate for treating high flow rates (at the expense of the production of huge amounts of metal-contaminated sludge that are poorly valuable). For the decontamination of water sources at drinkable levels, membrane techniques are more appropriate, but these techniques are frequently very expensive, and are preferred for the treatment of limited flow rates with low initial metal concentrations. Extractant impregnation of porous resins has also been investigated for metal removal; the immobilization of the extractant prevents the release and the loss of hazardous and expensive reagents with optimized transfer properties (driven by the porosity of the supports [3–5]). This is an intermediary technique between solvent extraction process and sorption on functional resins. Sorption processes using ion-exchange or chelating resins [6,7], carbon-based sorbents [8,9], inorganic supports [10–13] or biosorbents [14–18] have attracted great attention from both the research community and industrial sectors, especially for the treatment of low-concentration effluents or as polishing techniques.

Chitosan (aminopolysaccharide) and alginate are emblematic examples of supports used for metal recovery from dilute solutions. They are mainly extracted from marine resources (shrimp shell and algal biomass, respectively). These biopolymers are very versatile both physically (elaborating different shaping and conditionings) and chemically (reactivity of functional groups for chemical reaction and grafting of specific reactive groups) [19–24]. Chitosan is characterized by the presence of hydroxyl groups (providing hydrophilic behavior) and amine groups, which are highly reactive for metal binding. The sorption of metal ions may proceed through: (a) chelation of metal cations on electronic doublet of N (from free amine groups) in near neutral solutions, or (b) electrostatic attraction and ion-exchange mechanisms for the removal of metal anions on protonated amine groups in acidic solutions [25]. Chitosan is usually characterized by weak porosity (except when hydrogels are dried using expensive procedures such as drying under supercritical CO_2 conditions to form aerogels [26–28]); therefore, in order to reduce diffusion limitations, it is preferable to use small-size particles at the expense of increasing difficulties in solid/liquid separation. To avoid these problems, a solution may consist of incorporating magnetic nanoparticles in the hydrogels: magnetic separation improves the recovery of magnetic microparticles at the end of the sorption (resistance to intraparticle diffusion being limited by the decreasing in diffusion path through small particles) [29–31]. This is the strategy adopted in the current work. In a first step, magnetic chitosan microparticles were synthesized. To increase their reactivity (density of reactive groups, pH range for application, etc.), the support was modified by grafting additional functional groups. Several studies have shown interest in increasing the density of amine groups (polyethyleneimine grafting, for example), or inserting carboxylic groups (modulation of metal affinity, and pH effect), among other chemical modifications. Grafting amino acids onto chitosan backbone has been recognized as a promising technique for developing enhanced sorbents [32–36]. In this study, glycine (one of the simplest and cheapest amino acid) is immobilized on magnetic chitosan microparticles through the insertion of epichlorohydrin (acting both as a crosslinking agent for reinforcing the stability of the polymer and as a reactive spacing

arm). The sorbent (G@MChs) is characterized (SEM, FTIR spectroscopy, titration) before investigating its sorption properties for the recovery of Hg(II), Ni(II) and Zn(II) from aqueous synthetic solutions; the effects of pH, sorbent dose are determined before investigating uptake kinetics, sorption isotherms, metal desorption and sorbent recycling, and selectivity issues. These metals are representative of common hazardous metal ions having different levels of toxicity: in drinking water the guidelines are 70 μg Ni L^{-1}, and 6 μg Hg L^{-1} ([37]); WHO did not set guidelines for Zn in drinking water (at the levels found in this type of water bodies). In a second step, the sorbent is tested for the treatment of tailing leachates (produced from Egyptian mining resources). The leachates were pre-treated with pH control and sorption onto DOWEX 50X8 ion-exchange resin (for rare earth elements recovery, REE) before being treated by sorption onto G@MChs.

2. Materials and Methods

2.1. Materials

Chitosan (90.5% deacetylation degree) was supplied by Sigma-Aldrich (Merck KGaA group, Darmstadt, Germany), Glycine (>99.0%), and acetic acid were supplied by Biochem Chemopharma (Montreal, QC, Canada). Epichlorohydrin (>98%) and ethanol were purchased from Fluka AG (Buchs, Switzerland). Stock metal solutions (1 g L^{-1}) were prepared by dissolving in Milli-Q water salts of $HgCl_2$ (supplied by Carlo Erba Reagents srl, Cornaredo, Italy), $ZnCl_2$ and $Ni(NO_3)_2{\cdot}6H_2O$ (supplied by PanReac AppliChem, ITW Group, AppliChem GmbH, Darmstadt, Germany). DOWEX 50X8 cationic ion-exchange resin (supplied by Dow Chemical, Midland, MI, USA) was used for REE extraction from leachates. Working solutions were prepared by appropriate dilution of the stock solution; the pH was controlled using 0.1–1 M HCl or NaOH solutions prior to sorption experiments.

2.2. Synthesis of Sorbent

2.2.1. Preparation of Magnetic Chitosan Microparticles (MCh)

The Massart method was adapted for preparing magnetic chitosan microparticles. The one-pot synthesis proceeded by the hydrothermal co-precipitation of Fe(II) and Fe(III) salt [38]. Four grams of chitosan was dissolved in 200 mL of acetic acid solution (20%, *w*/*w*). Iron(II) ($FeSO_4{\cdot}7H_2O$, 6.62 g) and iron (III) ($FeCl_3$, 8.68 g) precursors were added to the chitosan solution, at 40 °C; the pH of the mixture was controlled to ~10 using 2 M NaOH solution. The hydrothermal precipitation produces dark magnetic chitosan microparticles (MCh), which were collected by magnetic separation (~17 g).

2.2.2. Activation of MCh Microparticles (MChs)

To reinforce the chemical stability of the composite, the material was mixed with 150 mL of an aqueous ethanol solution (1:1) and 1.5 mL epichlorohydrin; the pH was controlled to ~9.5, and heated under reflux at 90 °C for 5 h. To remove unreacted reagents and washed-up ethanol, the mixture was intensively rinsed with Milli-Q water and air-dried overnight to produce MChs (~17 g).

2.2.3. Insertion of Spacer Reactive Group (MChs*)

As a first step in the glycine grafting ([32]), the activated material was modified by insertion of reactive spacer arms to produce MChs*. The material was dispersed into 150 mL of water/ethanol (1:1) and 1.5 mL of epichlorohydrin, under reflux for 5 h. Afterward, the spacer arm-grafted material (~24 g) was magnetically separated and dried overnight.

2.2.4. Grafting of Glycine (G@MChs)

Finally, glycine (16 g) was dissolved into 250 mL of Milli-Q water; the pH was controlled to ~9.5. The activated material was dispersed into the solution and the mixture was maintained under agitation for 6 h under reflux at 90 °C. The sorbent (~36 g) was collected by magnetic separation, extensively rinsed with water before being freeze dried

at −99.6 °C under a pressure of 11 µbar. Scheme 1 summarizes the different steps in the process of sorbent manufacturing.

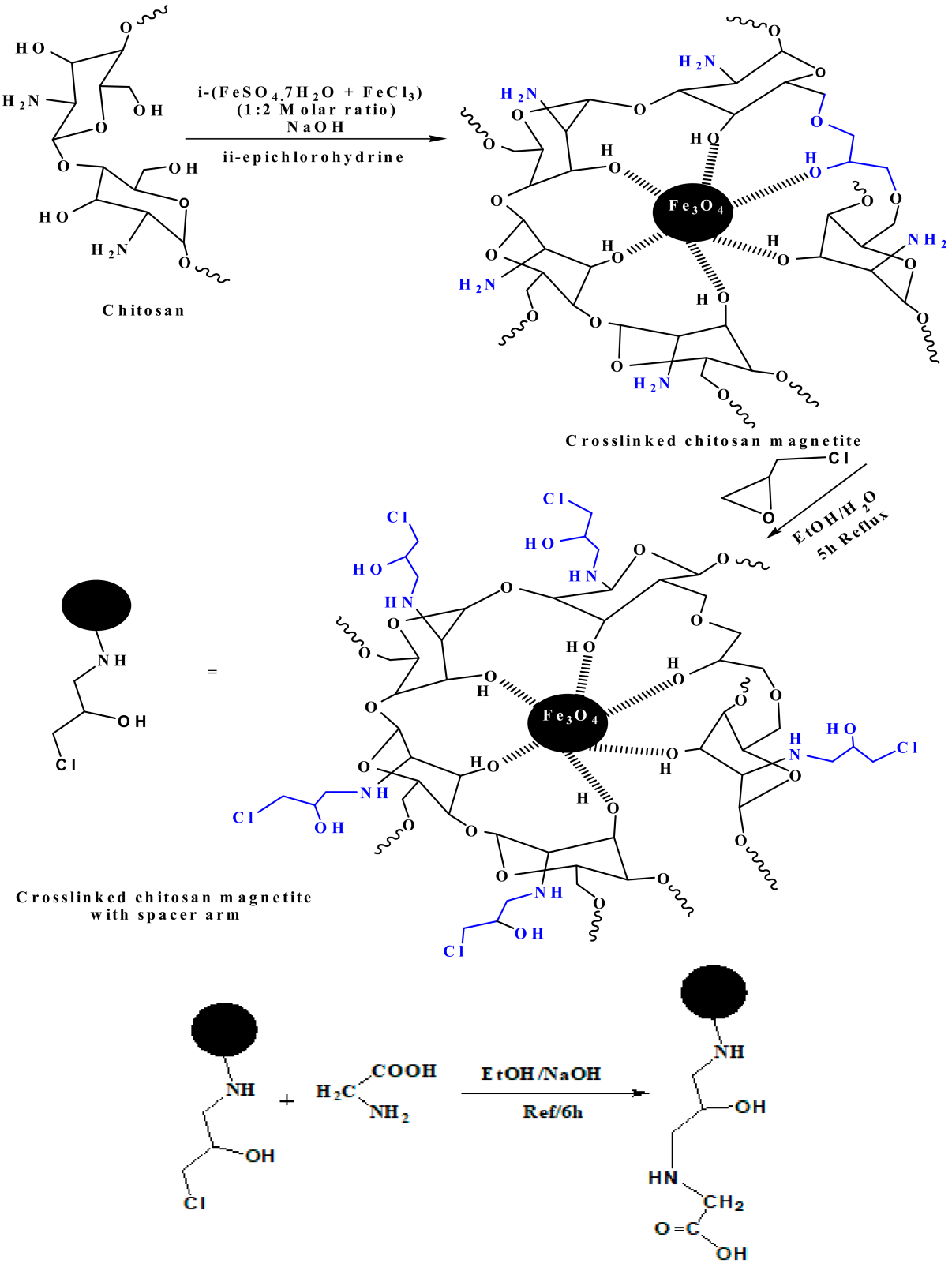

Scheme 1. Synthesis procedure for the preparation of G@MChs.

2.3. Characterization of Sorbent

Scanning electron microscopy was used for the characterization of the surface of sorbent particles. Observations were performed on a Quanta FEG 200 (FEI, Merignac, France, Thermo Fischer Instruments). The semi-quantitative analysis was performed using an energy dispersive X-ray analyzer (Oxford Instruments France, Saclay, France) with samples collected from the sorbent loaded at pH 5.5, with solutions containing a metal concentration of 0.3 mmol L^{-1} and a sorbent dose (SD) of 1 g L^{-1}. The same conditions were selected for loading the sorbent for FTIR spectrometer analysis (equipped with an ATR tool). The analysis of nitrogen content was carried out using the volumetric titration method reported by Donia et al. [39]. A fixed amount of sorbent (m = 50 mg) was dispersed into 50 mL (V, L) of 0.05 M HCl solution (C_0), for 15 h. The residual concentration of HCl (C_1) was titrated by 0.05 M NaOH solution (and phenolphthalein as the indicator). The molar concentration of amine groups in the sorbent (n, mmol g^{-1}) was calculated by: $n = (C_0\text{-}C_1) \times V/m$.

The pH_{PZC} of the sorbent was determined by the pH-drift method [40]. A fixed amount of sorbent was mixed with a solution at fixed pH_0 values using 0.01 M and 0.1 M NaCl salt as background. The equilibrium pH (pH_{eq}) was measured after 48 h of agitation (at 150 rpm). The pH_{PZC} corresponds to the pH value verifying $pH_0 = pH_{eq}$.

2.4. Sorption Tests

2.4.1. Experimental Procedures for Sorption and Desorption

Sorption tests were performed in batch system. The solution (volume, V, L) containing fixed initial concentrations (C_0, mmol L^{-1}), at selected pH values (pH_0), was mixed with a fixed amount of sorbent (m, g), under 150 rpm agitation. The sorbent dose (SD= m/V, g L^{-1}) was varied (when relevant) or set to 1 g L^{-1}. The specific experimental procedures are systematically reported in the caption of the Figures (see below). The pH was not controlled during the sorption process, but the final pH (pH_{eq}) was monitored using CyberScan 6000 pH-meter (Eutech Instruments, Nijkerk, The Netherlands, part of Thermo Fisher Scientific, Inc.). After magnetic solid/liquid separation of collected samples (variable time for kinetics, 24 h for equilibrium experiments such as isotherms and so on), the residual concentrations (C_{eq}, mmol L^{-1}) were determined using an inductively coupled plasma atomic emission spectrometer ICP-AES ACTIVA M (HORIBA JOBIN YVON, Longjumeau, France). The sorption capacity (q_{eq}, mmol g^{-1}) was calculated by the mass balance equation: $q_{eq} = (C_0\text{-}C_{eq}) \times V/m$. Similar experiments were applied for the study of sorption from multi-component solutions (the pH was set to 5.5), or for the treatment of industrial effluents (tailing leachates).

Acidic urea solutions were used for metal desorption from metal-loaded sorbents [41]. A 0.3 M urea solution (with pH controlled to ~2.7 with sulfuric acid solution) was used for the desorption step. The contact time was set to 24 h, under 150 rpm agitation. The released concentration allowed calculating the desorption yield (DE, %). For the tests of sorbent recycling (3 successive cycles), a rinsing step was systematically processed; the sorption capacities and sorption efficiencies were compared with the initial performances. To evaluate the stability of the sorbent, the FTIR spectrum of the sorbent after metal sorption and desorption was compared with the spectrum of pristine sorbent.

2.4.2. Modeling of Experimental Data (Uptake Kinetics and Sorption Isotherms)

Conventional methods were used for the modeling of sorption properties: (a) uptake kinetics was modeled using the pseudo-first-order rate equation (PFORE), the pseudo-second-order rate equation (PSORE) and the Crank equation (RIDE), (b) sorption isotherms were fitted by the Langmuir, the Freundlich and the Sips equations. The relevant equations are summarized in Table S1a,b, respectively (see Supplementary Information). The parameters were determined using non-linear regression analysis and the quality of the fits was evaluated and compared using the determination coefficient (i.e., R^2) and the Akaike Information Criterion (AIC, see Table S1b).

2.5. Ore Characterization and Leaching Operations

Gibbsite bearing shale ore material was collected from Abu Thor mining area in the district of Abu Zeneima locality (South Sinai Governorate, Sinai, Egypt). Major and economic elements were analyzed according the methods reported by Shapiro [42]. The samples were previously crushed (i.e., −200 mesh) and quartered. Calcium and Mg were determined by titration method using EDTA and Eriochrome black T as the indicator, respectively. Al_2O_3, SiO_2, and Fe_2O_3 (total) were measured using spectrometric analysis, Na_2O and K_2O were quantified using flame photometry. The index of rare earth elements (total REEs) was measured using UV-Visible spectrometry (Shimadzu UV-160, Shimadzu Scientific Instruments, Kyoto, Japan) [43] in the presence of arsenazo III (0.015%, *w*/*w*), at the wavelength λ: 654 nm. Trace elements corresponding to Cu, Zn, V, and Ni were determined at wavelengths 365.4, 334.4, 271.5, and 360.1 nm, respectively, by atomic absorption spectrometry (Pye Unicam Solaar 969, Pye Unicam, Cambridge, UK). Uranium was measured using oxidometric titration method by NH_4VO_3, in the presence of sodium salt of diphenyl amine-4-sulfonic acid as the titration indicator [44].

The Abu Thor mining area is characterized as a sedimentary basin; local ores are characterized by high contents of silica, aluminum, iron, calcium, and magnesium, with levels of 34.15%, 19.04%, 11.43%, 7.11%, and 4.18%, respectively. The chemical constituents of this ore are reported in Table S2. In addition to these major elements, the ores are characterized by important levels of base metals (Cu, Zn, Ni, Co, Cd and V), uranium (about 419 ppm), and REEs (about 1098 ppm). This ore is relatively complex to treat for the selective recovery of valuable metals because of the diversity of metals and the relatively high metal contents.

Several leaching agents were tested (i.e., sulfuric acid, hydrochloric acid, and nitric acid) and alkaline (carbonate and bicarbonate solutions). The optimum condition was achieved by using an agitated tank reactor, with sulfuric acid solution (100 g L^{-1}; i.e., ~1 mol L^{-1}), a solid/liquid ratio close to 1/3. Leaching was performed at room temperature, under agitation for 3 h. A pre-treatment was operated using DOWEX 50X8 cationic commercial resin at pH 4. The residual solution was tested for polishing treatment using synthesized sorbent. After filtration of collected pre-treated samples, the concentration of leached metal ions was analyzed. Sorption tests were carried out using the same experimental procedure as those used for sorption from synthetic solutions.

3. Results

3.1. Characterization of Sorbent

3.1.1. Surface Morphology

Figure 1 shows that the sorbent has a very irregular rough surface. Bindu and Mohanan [45] compared the effect of the crosslinking of magnetic chitosan materials on the morphology of the supports (for enzyme immobilization). They showed that the different crosslinking agents (including epichlorohydrin) converted the smooth, flat and dense morphology of magnetic chitosan particles into rougher and porous surfaces. Chitosan-embedded nanoparticles (roughly spherical objects) are incorporated into a scaffold structure with some tabular objects (leaflets).

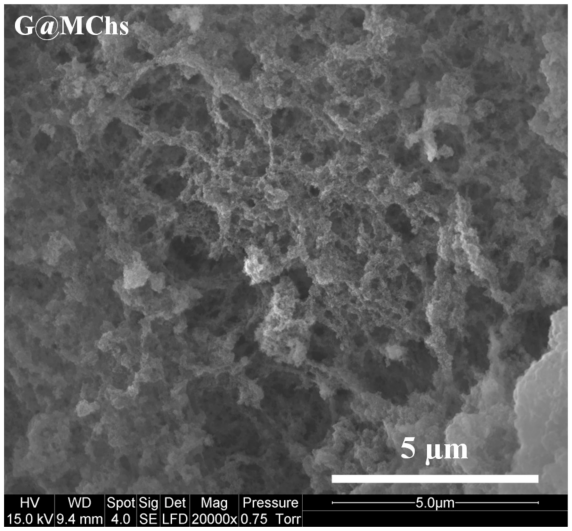

Figure 1. SEM micrograph of G@MChs.

3.1.2. Chemical Characterization—FTIR spectroscopy

Characterization of synthesized materials: The comparison of FTIR spectra confirms the incorporation of magnetite nanoparticles with the appearance of a peak at ~560 cm^{-1} (Fe-O-Fe stretching in Fe_3O_4) (Figure 2).

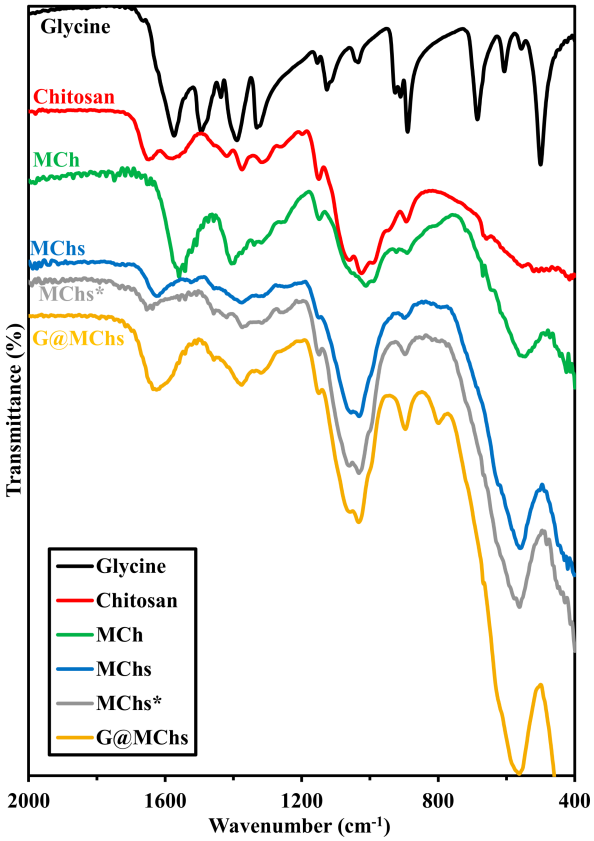

Figure 2. FTIR spectra of glycine, chitosan, and G@MChs sorbents (and intermediary compounds: MCh, magnetic chitosan; MChs, crosslinked magnetic chitosan; MChs*, and activated crosslinked magnetic chitosan with spacer arms) in the wavenumber range: 2000–400 cm^{-1}.

Table S3a–e report the assignments of the FTIR main peaks of reagents (glycine and chitosan), intermediary compounds, and the sorbent. All the intermediary products show an FTIR fingerprint close to the reference spectrum of chitosan, with the exception of the double band appearing in the range 1700–1500 cm^{-1}. Indeed, for raw chitosan, two bands are observed at 1648 and 1578 cm^{-1}: C=O stretching (amide I) and –NH bending, respectively. With the incorporation of magnetite (MCh), the amide I band apparently disappears and the absorbance of amine groups largely predominates (at 1558 cm^{-1}). After epichlorohydrin crosslinking (MChs) and activation with spacer arms (MChs*), on the other hand, the predominating peak is shifted toward higher wavenumbers (i.e., 1624 and 1653 cm^{-1}, respectively). Epichlorohydrin is supposed to graft (or crosslink) polymer units on hydroxyl groups of chitosan backbone [46] (formation of C-O-C bonds in case of interchain bonding and/or formation of C-Cl bonds in case of free ending grafting). The C-O-C bond is supposed to appear in the range 1150–1050 cm^{-1} [47]; herein, this is hidden by the contribution of the carbohydrate ring. The C-Cl bond is usually detected in the range 800–700 cm^{-1}; this vibration is not detected on MChs and MChs* spectra. After the immobilization of glycine onto the activated composite, two main differences are observed: (a) the appearance of a peak at ~796 cm^{-1}, and (b) the widening of the broad band 1700–1500 cm^{-1} (probably due to the contribution of the carboxylate functional group of glycine, at 1574 cm^{-1}). These successive changes demonstrate the incorporation of magnetite nanoparticles and the grafting of glycine on the chitosan backbone (through two successive steps of reaction with epichlorohydrin to crosslink and activate the support, respectively).

Characterization of metal ion interactions with G@MChs: here, the sorption of metal ions hardly changes the FTIR fingerprints (Figure 3).

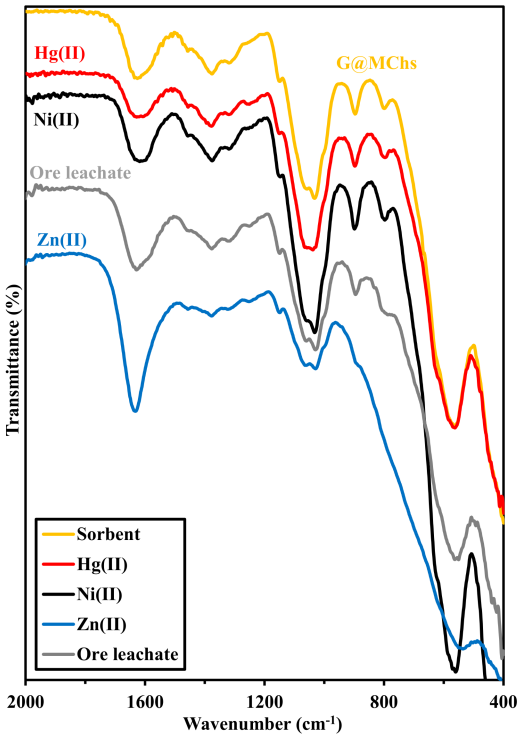

Figure 3. FTIR spectra of G@MChs sorbent before and after Ni(II), Zn(II), Hg(II) and after treatment of ore leachate, in the wavenumber range: 2000–400 cm^{-1}.

The most significant changes are observed at around 1600 cm^{-1}. The band is relatively large, probably due to the FTIR contribution of different reactive groups (amine, carboxylate). With metal sorption, the width of the band is modified, because the binding on these reactive groups shifts the wavenumber and/or modify the intensity of the relative contributions. In the case of Ni(II) and Hg(II), the group contributing at ~1595 cm^{-1} ap-

pears to be reinforced. On the contrary, for Zn(II), the width of the band is considerably reduced and the peak is centered around ~1632 cm^{-1} (reduction of the contribution of the FTIR component at lower wavenumber). The other significant change is identified at low wavenumber (below 850 cm^{-1}). The FTIR spectra are very similar for the sorbent before and after sorption of either Ni(II) and Hg(II), while for Zn(II) a much greater absorbance is observed between 600 and 850 cm^{-1}: the well-resolved peak at ~795 cm^{-1} is masked by a broad band of absorption. These results tend to confirm that the binding of the three metal ions does not follow the same mechanism, with Zn(II) being differentiated from Ni(II) and Hg(II). This difference cannot be directly correlated with the classifications reported by Pearson's rules (Hard and Soft Acid Base theory, HSAB [48]). Indeed, Ni(II) and Zn(II) are members of the borderline class, contrary to Hg(II) (classified among soft acids, which have greater affinity for soft bases, i.e., poor affinity for O- and N-bearing ligands).

These changes tend to demonstrate that the binding of the heavy metals mainly occurs on the carboxylate and amine groups holding onto the glycine moiety, or directly on the remaining free amine groups of the biopolymer. Scheme 2 illustrates the mechanisms involved in metal binding using G@MChs (as well as the desorption mechanism).

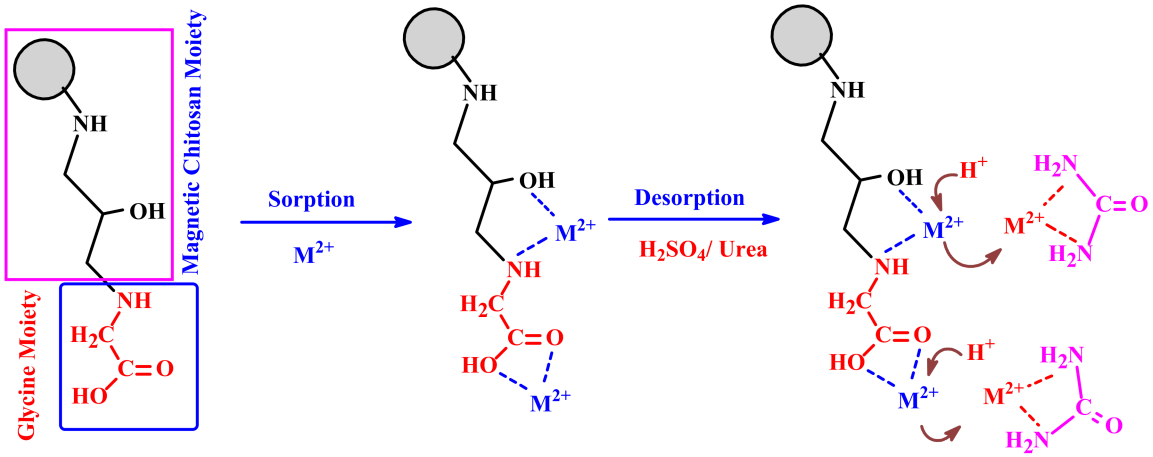

Scheme 2. Tentative mechanisms for the sorption of metal cations onto G@MChs and desorption from metal-loaded sorbent.

After metal desorption, the FTIR spectrum of the sorbent is partially restored (Figure S1, see Supplementary Information). The main difference is associated with the disappearance of the peak at 796 cm^{-1}, whose intensity for the regenerated material is considerably decreased (hardly detected).

3.1.3. pH_{PZC}—pH-Drift Titration

Figure S2 shows the application of the pH-drift method for the determination of the pH_{PZC} of the sorbent. The analysis was performed with two concentrations of background salt (i.e., 0.01 M and 0.1 M NaCl solutions). The pH_{PZC}, which corresponds to $pH_0 = pH_{eq}$, varies between 8.07 and 8.76; the value decreases with the concentration of the background salt because of the charge screening effect. It is noteworthy that this variation is more marked than usually (where ΔpH_{PZC} rarely exceeds 0.2 pH unit). This means that the sorbent is totally protonated in acid solutions. The higher pH increase is observed at pH_0 4; logically, the protonation decreases with increasing the pH. The main constituents of G@MChs are crosslinked chitosan and glycine moieties. Sorlier et al. [49] reported that the pK_a of amine groups in chitosan varies with the deacetylation degree of chitosan and the charge neutralization; for most conventional (commercial) chitosan, the pK_a is close to 6.5, while the pK_a values of glycine are 2.34 and 9.6 for carboxylic group and amine group, respectively [50]. The grafting of glycine onto crosslinked chitosan (magnetite-supported) appears to make the acid–base properties of the composite closer to those of the amine moiety of glycine (compared to carboxylic group end).

The titration of G@MChs allows the determination of the nitrogen content of the composite: 1.84–1.96 mmol N g^{-1} (i.e., 2.57–2.74%, *w*/*w*). In chitosan, the amine groups represent ~5–5.5 mmol N g^{-1}. This means that the fraction of magnetite in the composite is roughly close to 50%. Actually, the theoretical content (based on the amount of reagents used in the synthesis) and the effective titration (for N content) show a large dispersion (meaning that the magnetite content is in the range 50 ± 14%).

3.2. Sorption Tests

3.2.1. Effect of pH

The pH of the solution influences both the speciation of metal ions (including their ionic charge) and the surface charge of the sorbent. These characteristics directly influence the attraction vs. repulsion mechanisms in the interaction of metal ions with sorbent surface. The sorption properties were carried out in the range pH_0: 3–6.5. The determination of pH_{PZC} (Section 3.1.3.) showed that the sorbent is positively charged in this pH range. The protonation of reactive groups increases with the acidity of the solution; the repulsion effect of protonated sorbent surface with metal cations is thus decreasing when the pH increases. This can explain the general trend observed for the three metal ions: the sorption efficiency increases with equilibrium pH (Figure 4), especially between pH 3 and pH 5–6, above which the sorption efficiency tends to stabilize.

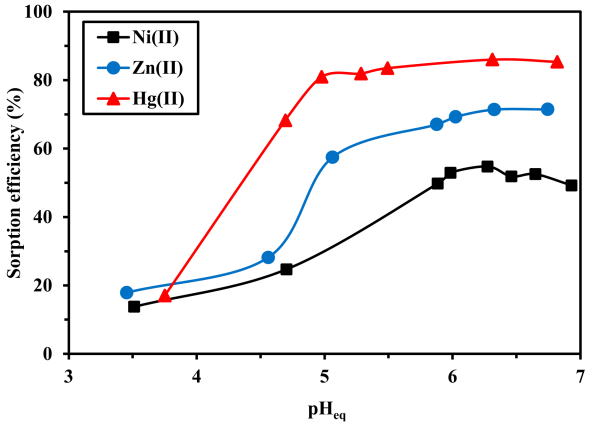

Figure 4. Effect of pH on the sorption efficiency for Ni(II), Zn(II), and Hg(II) using G@MChs (C_0: 0.3 mmol L^{-1}; sorbent dose, SD: 1 g L^{-1}; T: 21 ± 1 °C; time: 480 min; agitation speed: 150 rpm).

Figure S3 shows the speciation diagram of the three metal ions (under the experimental conditions used for the study of pH effect, taking into account metal salt, acid and base used for pH control); the speciation diagram was calculated using Visual Minteq [51]. Nickel is present in its free form in the whole range of pH; other species represent less than 0.5%. Zinc behaves similarly to Ni(II); between pH 3 and 6.5, Zn^{2+} exceeds 99.5%, while other species are negligible except $ZnCl^+$ (about 2.1% at pH 2) and $ZnOH^+$ (less than 0.9% at pH 7). These metal cations are bound by complexation; the strong competition of protons limits the sorption, which progressively increases with pH. Actually, for the two metal ions, the sorption capacity begins to significantly increase above pH_{eq} 4.5 (pH_0: 3.7–4.7). The case of Hg(II) in Figure 4 differs slightly because a strong increase (almost linear) in metal sorption is observed even at pH_0 3.5 (pH_{eq} 3.7). Actually, the speciation diagram shows that mercury is mainly present as a neutral species (mainly $HgCl_2$, up to pH ~6, completed above with HgClOH and $Hg(OH)_2$), with the exception of about 10% of $HgCl_3^-$ anionic species at pH 2. Anionic species can be readily bound onto protonated reactive groups, though at high acidity the counter ions of the acid (herein chloride ions) may strongly compete with $HgCl_3^-$ for binding. At higher pH values, the repulsive effect of protonated amine groups reducing the sorption of Ni(II) and Zn(II) does not inhibit the binding of $HgCl_2$ (and other neutral species). Consequently, the density of counter anions bound onto

the reactive groups decreases; therefore, the reactive groups become more available for metal complexation.

Sorption processes may change the pH of the solution dues to proton binding or release by the sorbent. The speciation of the metal ions (which may change during the sorption by displacement of the equilibrium of complexation) may also affect the final pH of the solution. The comparison of initial and equilibrium pH may be helpful for understanding the mechanisms involved in metal binding. Figure S4 shows these comparisons. Whatever the metal considered, the final pH is systematically increased during the sorption and the ΔpH may reach up to 1–1.5 pH unit (especially for nickel). Actually, the pH variations globally follow the trend: Hg(II) < Zn(II) < Ni(II), inversely with the ranking in sorption efficiency Hg(II) [~86%] > Zn(II) [~71%] > Ni(II) [~55%]. The sorption of mercury consumes less protons than the binding of other divalent cations.

These results offer a first indication as to the preference of the sorbent for metal ions according the series: Hg(II) > Zn(II) > Ni(II). This ranking can be correlated with the decreasing order of K_s values, softness parameter, and hydrated radius (Table S4). It is noteworthy that the sorbent may contain amine groups (from chitosan and glycine) and carboxylate groups (from glycine). The immobilization of glycine onto MChs may consume some of these groups. The O-ligand in carboxylate is considered a hard base, while N-ligand in amine and substituted amine groups is classified among intermediary bases. Pearson's rules [48] suppose that hard acids preferentially react with hard acids (and reciprocally, soft bases with soft acids). Zn(II) and Ni(II) metal ions are borderline acids; they are supposed to be preferentially bonded to amine groups; the order of preference is probably modulated by their relative softness. On the other hand, Hg(II) is classified as a soft acid; its speciation (and the formation of neutral species) is predominantly related to the control of interactions rather than the pure Hard/Soft effect.

3.2.2. Effect of Sorbent Dose

Obviously, increasing the sorbent dose improves the recovery of metal ions (Figure S5); however, this beneficial effect is largely counterbalanced by a drastic decrease in the sorption capacity. Increasing the sorbent dose does not allow optimizing the rational use of the sorbent. Depending on the target of the process, decontaminating the effluent (lowest residual concentrations requested) requires the use of a high sorbent dose, while valorization of metals requires concentration of the metal in the sorbent (meaning using lower sorbent doses). For the further experiments, a sorbent dose of 1 g L^{-1} was selected as a good compromise between these two objectives.

3.2.3. Uptake Kinetics

Mono-component solutions: Figure 5 compares the kinetic profiles for the sorption of Ni(II), Zn(II) and Hg(II) using G@MChs. A contact time of 60 min is sufficient for reaching the equilibrium. Residual concentrations follow the expected trend in terms of preference: Hg(II) > Zn(II) > Ni(II). The initial slopes of the plots of relative concentrations are very close for Hg(II) and Zn(II), and larger than for Ni(II). Pearson's rules also apply to kinetic behavior in terms of comparative reactivity. This is consistent with the current trends (although the study of the pH effect showed that, for Hg(II), the speciation effect occults the impact of HSAB concepts).

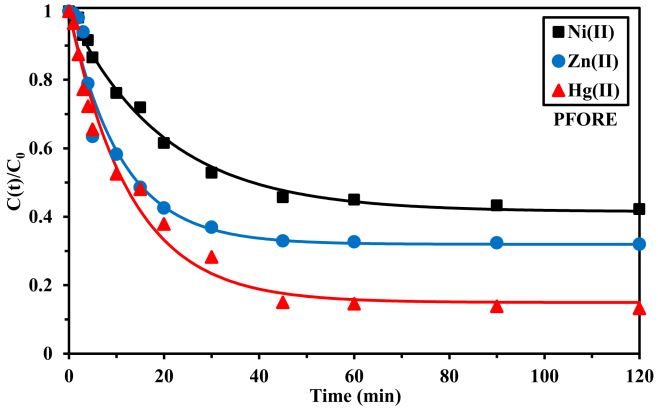

Figure 5. Uptake kinetics for Ni(II), Zn(II) and Hg(II) using G@MChs for single-component solutions—modeling with the PFORE (C_0: 0.3 mmol L^{-1}; pH_0: 5.5; pH_{eq}: 5.75 (Ni), 5.80 (Zn), and 6.01 (Hg); Sorbent dose, SD: 1 g L^{-1}; T: 21 ±1 °C; time: 300 min (equilibrium reached before 120 min); agitation speed: 150 rpm).

The equilibrium time is relatively fast; however, taking into account the size of sorbent particles, one would expect the sorption to be faster. Different modes of resistance to mass transfer (including bulk diffusion, film, and intraparticle diffusions) may contribute to the control of uptake kinetics. In addition, the proper reaction rate may play a role in this control. By extrapolation to homogeneous reactions, the kinetic profiles can be modeled using the pseudo-first- and pseudo-second-order rate equations (summarized in Table S1, in addition to the Crank equation that can be used for approaching the resistance to intraparticle diffusion). In the case of heterogeneous systems, the rate coefficients obtained in the fitting of experimental profiles should be considered as apparent rate constants (which implicitly take into account the resistances to diffusion). Table 1 summarizes the fitted parameters for the different models and the three metal ions (together with the statistical criteria; i.e., R^2 and AIC). It is apparent that the kinetic profiles for Ni(II) and Zn(II) are preferentially fitted by the PFORE, while Hg(II) sorption better follows the PSORE. In Figure 5, the solid lines represent the fitting of experimental curves with the PFORE; the fittings with the PSORE and the RIDE are reported in Figures S6 and S7, respectively. The PSORE is frequently associated with chemisorption; however, Simonin [52] and Hubbe et al. [53] pointed out the importance of the appropriate selection of experimental conditions for giving sense to this assertion. Hubbe et al. [53] commented that the concentration and the sorbent dose must be selected to avoid the strong variation of the concentration of the adsorbate in the solution for correctly attributing the binding mechanism to chemisorption (with best PSORE fitting). Alternatively, the fitting of the kinetic profile with the PSORE only reflects the control of resistance to intraparticle diffusion. The values of the $q_{eq,1}$ (PFORE) are remarkably close to the experimental values of the sorption at equilibrium. The apparent rate coefficients (i.e., k_1) vary in the range 0.05–0.09 min^{-1}, according the series: Zn(II) > Hg(II) > Ni(II).

The application of the Crank equation (RIDE) shows lower quality for fitting the experimental profiles. However, it is possible to approach the order of magnitude of the apparent diffusion coefficients of target metal ions in G@MChs (i.e., ~2–5 × 10^{-12} m^2 min^{-1}), which are four order of magnitude lower than their molecular diffusivity in water (i.e., ~4–5 × 10^{-8} m^2 min^{-1}). The intraparticle diffusivity coefficients follow the trend: Zn(II) > Ni(II) > Hg(II), which is not directly correlated with the ionic size of hydrated species (Hg(II) > Zn(II) > Ni(II)). Again, the speciation of metal ions (especially for Hg(II)) may interfere with the effective size of diffusing species. The relative values of the intraparticle diffusion coefficients (compared with molecular diffusivity) mean that the contribution of resistance to intraparticle diffusion cannot be neglected.

Table 1. Ni(II), Zn(II) and Hg(II) uptake kinetics using G@MChs for single-component solutions—parameters of the models.

Model	Parameter	Ni(II)	Zn(II)	Hg(II)
Experimental	$q_{eq,exp.}$ (mmol g^{-1})	0.148	0.210	0.263
PFORE	$q_{eq,1}$ (mmol g^{-1})	0.150	0.210	0.258
	$k_1 \times 10^2$ (min^{-1})	4.99	9.13	7.70
	R^2	0.995	0.968	0.985
	AIC	−109	−78	−85
PSORE	$q_{eq,2}$ (mmol g^{-1})	0.184	0.243	0.297
	k_2 (L $mmol^{-1}$ min^{-1})	0.270	0.422	0.310
	R^2	0.986	0.955	0.991
	AIC	−94	−73	−93
RIDE	$D_e \times 10^{12}$ (m^2 min^{-1})	3.38	4.80	1.99
	R^2	0.979	0.946	0.984
	AIC	−85	−71	−84
	$D_0 \times 10^8$ (m^2 min^{-1})	3.97	4.22	5.08

Multi-component solutions: A complementary study of the uptake kinetics was performed on multi-component solutions (with equimolar concentrations) (Figure 6, Figures S8 and S9, and Table 2). The equilibrium time is unchanged (i.e., 60 min). Apparently, the presence of competitor ions strongly affects the kinetic behavior of Ni(II) and Zn(II); the profiles for these two metal ions almost overlap (contrary to mono-component profiles, Figure 5). The sorption capacities at equilibrium are quasi halved and the apparent rate coefficients reach intermediary values (0.068–0.062 min^{-1}) compared to mono-component kinetics. In the case of Hg(II), the impact of the other metal ions has a limited effect on sorption capacities at equilibrium (q_{eq} decreases from 0.26 to 0.21 mmol Hg g^{-1}; i.e., −18%). This is a first indication of the preference of G@MChs for Hg(II) vs. Ni(II) and Zn(II) (see below for extended study of selectivity issues). In addition, the apparent rate coefficient (i.e., k_1) slightly increases compared with mono-component solutions from 0.077 to 0.92 min^{-1}. Surprisingly, the modeling of kinetic profiles with the Crank equation shows an increase in the apparent diffusion coefficient (especially for Ni(II) and Hg(II), where the D_e values are doubled).

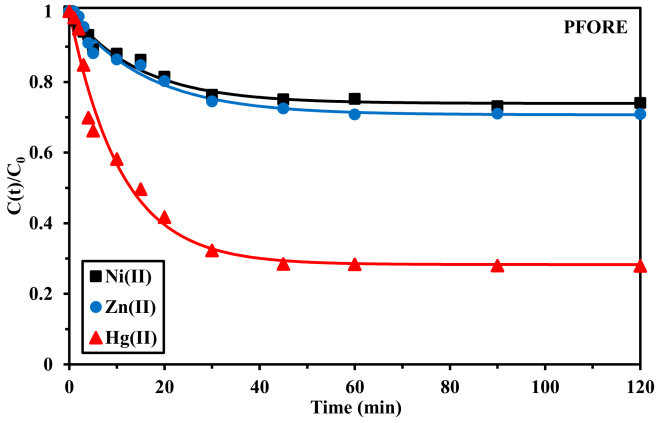

Figure 6. Uptake kinetics for Ni(II), Zn(II) and Hg(II) using G@MChs for multi-component solutions—modeling with the PFORE (C_0: 0.3 mmol L^{-1}; pH_0: 5.5; pH_{eq}: 5.75 (Ni), 5.80 (Zn), and 6.01 (Hg); Sorbent dose, SD: 1 g L^{-1}; T: 21 ±1 °C; time: h; agitation speed: 150 rpm).

Table 2. Ni(II), Zn(II) and Hg(II) uptake kinetics using G@MChs for multi-component solutions—parameters of the models.

Model	Parameter	Ni(II)	Zn(II)	Hg(II)
Experimental	$q_{eq,exp.}$ (mmol g^{-1})	0.070	0.097	0.216
PFORE	$q_{eq,1}$ (mmol g^{-1})	0.070	0.097	0.214
	$k_1 \times 10^2$ (min^{-1})	6.79	6.23	9.25
	R^2	0.980	0.977	0.980
	AIC	−114	−110	−86
PSORE	$q_{eq,2}$ (mmol g^{-1})	0.081	0.115	0.246
	k_2 (L $mmol^{-1}$ min^{-1})	0.985	0.608	0.445
	R^2	0.980	0.975	0.976
	AIC	−111	−100	−82
RIDE	$D_e \times 10^{12}$ (m^2 min^{-1})	6.38	6.17	4.44
	R^2	0.978	0.971	0.970
	AIC	−122	−108	−79

3.2.4. Sorption Isotherms

The sorption isotherms report the distribution of the adsorbate between liquid and solid phases, at fixed temperature, at a wide range of concentrations (Figure 7). The profiles for Ni(II) and Zn(II) are very close, indicating their similarity in sorption mechanism. The sorption capacity progressively increases with residual concentration, before reaching an apparent plateau; the maximum sorption capacities are close to 0.45 mmol g^{-1}. The sorption of mercury shows a different type of curve: the isotherm begins with steep initial slope that reflects a quasi-irreversible behavior (almost rectangular isotherm); the saturation plateau (more marked than for the other metal ions) is reached at $Ce_q \sim 1$ mmol Hg g^{-1}. The maximum sorption capacity is significantly lower than for Ni(II) and Zn(II) (i.e., 0.33 mmol Hg g^{-1}).

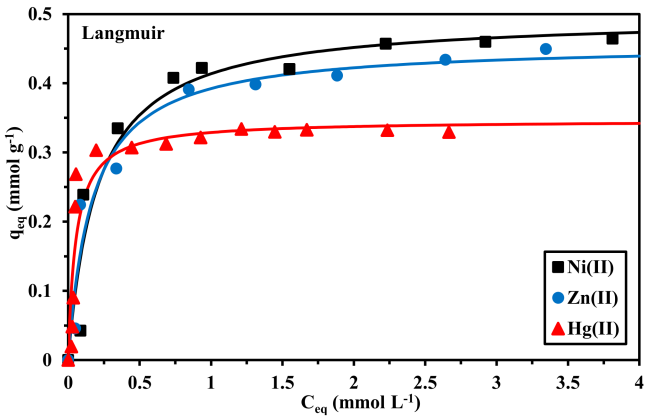

Figure 7. Sorption isotherms for Ni(II), Zn(II) and Hg(II) using G@MChs for single-component solutions—modeling with the Langmuir equation (C_0: 0.3 mmol L^{-1}; pH_0: 5.5; pH_{eq}: 5.75 (Ni), 5.80 (Zn), and 6.01 (Hg); sorbent dose, SD: 1 g L^{-1}; T: 21 ±1 °C; time: 60 min; agitation speed: 150 rpm).

The Langmuir, Freundlich and Sips equations were tested for modeling the isotherms (Table 3). The saturation plateau appearing in the figure suggests that the Langmuir or the Sips equations better fit the experimental profile than the Freundlich equation (which is a power-type function). This is confirmed by the statistical parameters in Table 3.

Table 3. Ni(II), Zn(II) and Hg(II) sorption isotherms using G@MChs—parameters of the models.

Model	Parameter	Ni(II)	Zn(II)	Hg(II)
Experimental	$q_{m,exp.}$ (mmol g^{-1})	0.465	0.449	0.332
Langmuir	$q_{m,L}$ (mmol g^{-1})	0.497	0.457	0.347
	b_L (L $mmol^{-1}$)	4.94	6.02	18.5
	R^2	0.938	0.959	0.888
	AIC	−58	−56	−90
Freundlich	k_F	0.370	0.348	0.308
	n_F	4.04	3.75	4.84
	R^2	0.857	0.917	0.762
	AIC	−50	−49	−79
Sips	$q_{m,S}$ (mmol g^{-1})	0.459	0.466	0.323
	b_S (L $mmol^{-1}$)	13.7	5.10	∞ *
	n_F	0.682	1.06	0.203
	R^2	0.947	0.959	0.993
	AIC	−55	−51	−129

* Quasi irreversible/rectangular isotherm (∞: $6.9 \cdot 10^6$).

The Langmuir equation best fits the experimental profile; except for Hg(II), where the Sips equation better fits the curve (but the corresponding affinity (infinite) has no physical significance). The Langmuir fits are presented as solid lines in Figure 7. The sorption capacities at saturation of the monolayer ($q_{m,L}$) are consistent with the experimental maximum sorption capacities. The greater affinity of the sorbent for Hg(II), already apparent from the initial steep slope, is confirmed by the values of the affinity coefficient (i.e., b_L): Hg(II) [18.5] >> Zn(II) [6] > Ni(II) [4.9]. The Langmuir equation is based on the sorption of the adsorbate as a monolayer, without interactions between sorbed molecules, and with homogeneous energy of sorption at the surface of the sorbent. Figure S10 shows the fitting of experimental profiles using the Sips equation (and the parameters summarized in Table 3); in the case of Hg(II), the Sips equation overestimates the sorption capacity in the highest curvature section of the curve (contrary to the Langmuir equation, which underestimates these values), making the isotherm rectangular.

Table 4 summarizes the sorption properties of a series of chitosan-based sorbents investigated for the binding of Ni(II), Zn(II), and Hg(II). Apparently, the sorption properties of G@MChs are significantly lower than these alternative materials.

The main advantage of the magnetite-supported sorbent is related to the relatively fast uptake kinetics, due the micron size of the sorbent particles (made possible by the readily magnetic separation of composite). It is important to report that the magnetite content is close to 50%; this means that the sorption capacities for the polymer coating are expected to be doubled, and more consistent with the values reported for alternative sorbents. It is noteworthy that for some outstanding sorbents, selected experimental conditions make the sorption properties doubtful because of the possible occurrence of precipitation phenomena.

Figure S11 compares the surface characterization of the sorbent after Ni(II), Zn(II) and Hg(II) sorption with pristine sorbent. It is apparent that the irregular surface of raw sorbent is smoothed after metal binding, especially for Ni(II) and Hg(II); small agglomerates are observed in these case with flaky structures. Similar surface modifications were observed with lead accumulation at the surface of Taro crop biosorbent [74].

Table 4. Comparison of Ni(II), Zn(II) and Hg(II) sorption properties (temperature, T, K; t_{eq}, min; $q_{m,L}$, mmol g^{-1}; b_L, L $mmol^{-1}$) for alternative chitosan-based sorbents.

Metal	Sorbent	pH_0	T	t_{eq}	$q_{m,L}$	b_L	Ref.
Ni(II)	MCSB	-	298	60	$3.9 \cdot 10^{-4}$ (a)	1160	[54]
	GLU-MCSB	-	298	60	$7.8 \cdot 10^{-4}$ (a)	5465	[54]
	Amino-thiocarbamate derivative of alginate, carboxymethyl chitosan and TiO_2	6.0	298	180	2.93	354	[55]
	Ion-imprinted seaweed-chitosan composite	7.0	298	1440	0.990 (b)	-	[17]
	Hydrazinyl amine magnetite-chitosan	5.0–5.1	298	1440	4.33	2.35	[56]
	Chitosan-vanillin	4.0	303	1440	0.324	30.6	[57]
	Magnetic chitosan hexyl acrylate (Mag-CSg-HA)	5.5	293	600	2.08	9.39	[58]
	Amidoximated chitosan/acrylamide/acrylonitrile/3-dimethylaminoallyl phosphonic acid	5.0	303	720	3.64	0.177	[59]
	Magnetic activated carbon/chitosan beads	6	298	360	1.85	13.5	[60]
	PVA/chitosan/ZnO-NH_2 nano-fiber	6	298	240	0.375	1.67	[61]
	4-aminobenzoic acid grafted chitosan	7	298	60	2.34	0.317	[62]
	Si/Fe nanostructures -chitosan polymer composites (CF4)	-	298	50	1.32	21.2	[63]
	G@MChs	5.5	293	120	0.497	4.94	herein
Zn(II)	EDTA-modified γ-MnO_2/Chs magnetic nanocomposite	6	298	110	2.08	5.69	[64]
	Carboxylate funct. chitosan copolymer (CFCCPeCOOH)	6	313	60	0.369	175.2	[65]
	Formaldehyde cross-linked chitosan	4	298	50	0.0048	3633	[66]
	4-aminobenzoic acid grafted chitosan	6	298	60	2.00	0.281	[62]
	Si/Fe nanostructures-chitosan polymer composites (CF4)	-	298	50	1.04	14.3	[63]
	G@MChs	5.80	293	120	0.457	6.01	herein
Hg(II)	Chitosan-pectin gel beads	7	298	160	1.04	21.5	[67]
	MCTP (c)	3.5	298	90	2.57	90.1	[68]
	β-Cyclodextrin-Chitosan	6	295	90	0.939	∞ (d)	[69]
	Amorphous aluminosilicate modified chitosan (G2.50/Ch)	8	298	60	0.865	26.7	[70]
	Hydrazide-micromagnetite chitosan derivative	5	295	2880	1.97	118.3	[71]
	Polyethyleneimine functionalized chitosan-lignin	5.5	303	360	3.42	9.63	[72]
	Amido-funct. carboxymethyl chitosan/montmorillonite (e)	5.5	303	250	9.00	263	[73]
	G@MChs	6.01	293	120	0.482	18.5	herein

(a) Adsorption from wastewater sample; (b) experimental values; (c) MCTP was constructed by introducing the poly (m-aminothiophenol) and chitosan onto the magnetic-mesoporous nanoparticle under tannic acid as a cross-linking agent; (d) ~6.5×10^6; (e) suspicion of precipitation (10 mmol L^{-1} at pH 5.5, Visual Minteq).

3.2.5. Effect of Temperature on Sorption Capacity

To evaluate the thermodynamic behavior of the sorbent, sorption tests were performed at increasing temperatures (for three different metal concentrations). Figure S12 shows that within this small temperature range, the sorption capacities hardly change with increasing temperature; in most cases (metal and initial metal concentration), the sorption capacity increases by less than 3%. The sorption is slightly endothermic. A larger range of temperature would be necessary to precisely evaluate the thermodynamic constants [75]; however, the variation observed between 20 and 37 °C (centered around conventional operational conditions) gives a first indication of the negligible impact of temperature on sorption performance.

3.2.6. Selectivity—Sorption from Multi-Component Solutions

The evaluation of the sorption of metal ions in complex solutions (involving different metal ions; herein Zn(II), Cd(II), Ni(II), Cu(II), Hg(II) and Pb(II)) is an important criterion in the design of sorbents. Indeed, the selectivity issue is critical for separating the metals in order to enhance their valorization. Sorption tests were performed from multi-component solutions with concentrations ranging between 10 and 200 mg L^{-1}, at pH 5.5.

Figure S13 shows the sorption isotherms obtained for the different metal ions from these multi-component solutions; the sorption isotherms are incomplete, the saturation

plateau was not reached for some of these metal ions (i.e., Pb(II), Ni(II) and Cu(II)). The sorption capacities can be roughly ranked according the series (compared for C_{eq} ~0.4 mmol L^{-1}): Hg(II) > Cu(II) > Pb(II) > Ni(II) > Zn(II) > Cd(II). The saturation of the sorbent has not been reached; therefore, the trend should be considered only indicative. The poor efficiency for cadmium may be explained by intermediary and hard base characteristics of the reactive groups (carboxylate and amine groups) on the sorbent, while cadmium is part of the strong acid metals. According to Pearson's rules, G@MChs (classified as intermediary/hard base) has preferential affinity for borderline and hard elements (mercury behavior does not follow this trend because the formation of chloro-mercuric species modulates this effect).

The selectivity coefficient is calculated as the ratio of distribution ratios:

$$SC_{Me1/Me2} = \frac{D(Me_1)}{D(Me_2)} = \frac{q_{eq,Me1} \times C_{eq,Me2}}{q_{eq,Me2} \times C_{eq,Me1}} \quad (1)$$

Cadmium being the metal with the lowest affinity for G@MChs, the selectivity coefficients were determined with reference to this metal in Figure S14 ($SC_{Cd/Cd}$ = 1); the different $SC_{Metal/Cd}$ values are compared for the different metal concentrations (10–200 mg L^{-1}). The selectivity order follows the trend: Hg(II)>>Pb(II)>>Cu(II)>>Ni(II)>>Zn(II). Except for Hg(II) (soft acid, whose behavior is controlled by the formation of chloro-species), the metal ions belong to borderline metals which are suspected to have higher affinity for intermediary bases (such as amine groups). It is noteworthy that this ranking is modified at low metal concentration where the order is reversed for Hg(II) and Pb(II)/Cu(II) (i.e., Pb(II) > Cu(II) > Hg(II)).

3.2.7. Metal Desorption and Sorbent Recycling

The rationale for using urea is based on the ability of this reagent to bind with metal cations. Combining urea with acidic solutions allows both reversing metal sorption (effect of unfavorable pH conditions) and favoring the competition effect between free urea and reactive groups at the surface of the sorbent for metal binding. Therefore, the tentative mechanisms of sorption and desorption are illustrated by Scheme 2.

Sorption performances (sorption efficiency and sorption capacity) were compared for three successive cycles for Ni(II), Zn(II) and Hg(II) (Figure 8). The most stable performance is observed for Hg(II), where the loss in sorption is less than 1.2% at the third cycle. On the other hand, the recycling of the sorbent has more impact on Ni(II) removal; the decrease in sorption reaches up to 9%. The desorption efficiency was not quantified; the slight decrease in sorption efficiency and sorption capacity at sorbent recycling may be explained by two causes: (a) the incomplete desorption of metals ions that contribute to the progressive saturation of the material, and (b) the partial degradation of the sorbent during the alternating sorption and desorption cycles. This deserves complementary investigation.

The stability of magnetite NPs in chitosan-based composites was investigated in acidic solutions [56,71]. After 24 h exposure to 0.5 M HCl solutions, the loss of iron (as a tracer of magnetite) did not exceed 1.1%. This is first evidence for sorbent stability. It is noteworthy that in this study, the acidic conditions are less "aggressive" than in previous tests (pH 2.7 and sulfuric acid solutions vs. pH ~1 and HCl solution). In addition, the FTIR characterization and the semi-quantitative EDX analysis confirmed the stability of the sorbent; herein, Figure S1 illustrates this stability.

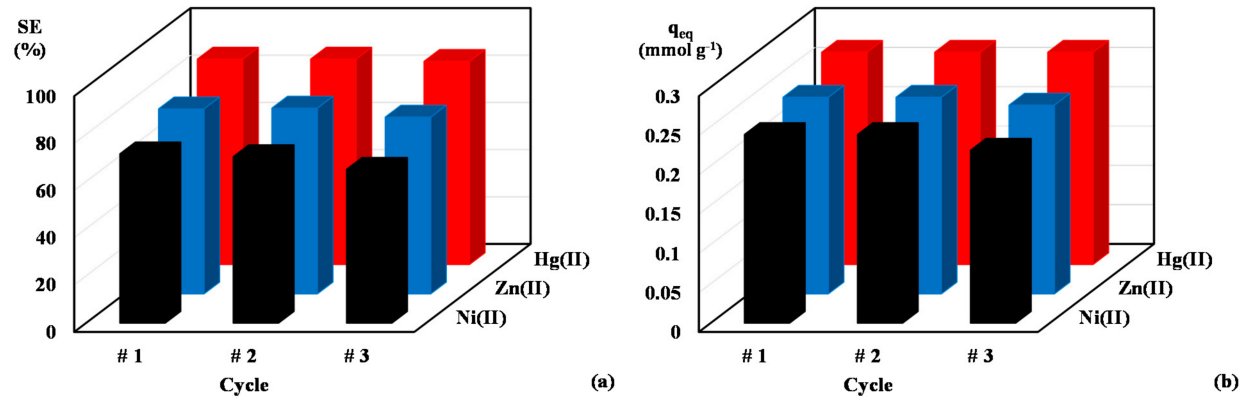

Figure 8. Sorbent recycling for 3 cycles—Sorption efficiency (SE, %) (**a**), and sorption capacity (**b**) (q_{eq}, mmol g^{-1}) (experimental conditions: identical to standard sorption experiments, see Figure 7).

3.3. Treatment of Tailing Leachates

The sorbent was tested for the treatment of the tailing leachate and further extraction of REEs using DOWEX 50X8 resin. This step recovered around 75% of total REEs and up to 38% of uranium leached from tailings. In addition, this pre-treatment process allowed the removal of 90% of cadmium and about 69% of nickel. Table S5 reports the composition of the ore leachate (before and after pH control to 4) and after sorption step. Figure S15 reports the sorption capacities for selected metals and the selectivity coefficients for these metals (with reference to Cd, as in Section 3.2.6.). For Al and Cu (whose initial concentrations were ~103.8 mmol Al L^{-1} and 14.58 mmol Cu L^{-1}), the occurrence of precipitation at pH 5.5 greatly overestimates the sorption capacities (Figure S15a). In the case of Fe(III), the initial concentration is close to 1.42 mmol Fe L^{-1}, making possible the formation of hydrocolloids that facilitate the recovery of the metal; the sorption capacity reaches up to 1.39 mmol Fe g^{-1}. Other than the three metal ions present in elevated concentrations (subject to hydrolysis and precipitation mechanisms), the other metal ions show sorption capacities below 1 mmol g^{-1}. The initial concentration of Zn(II) reaches up to 7.30 mmol Zn L^{-1}; this may explain the high sorption capacity (close to 0.99 mmol Zn g^{-1}). Nickel is another major element in the leachate (concentration: ~1.37 mmol Ni L^{-1}); the sorption capacity is close to 0.41 mmol Ni g^{-1}. Much lower sorption levels (below 0.1 mmol g^{-1}) are reported for other metal ions, which is consistent with their relative initial concentrations in the leachate. Apparently, the sorbent has a wide reactivity for different types of metal ions. The apparent selectivity coefficients (i.e., $SC_{metal/Cd}$) are relatively limited (varying between 3 and 0.3); these values are not sufficient to effectively separate these metals. It is noteworthy that the levels of concentration are drastically different, making the comparison of SC values only indicative of some trends in the preference of sorbent for given metal ions. High initial concentrations (large excess) may contribute to minimizing the SC values, while precipitation phenomena induce the overestimation of SC values (Al, Cu and to a certain extent Fe). The sorbent shows a preference for metal ions according to the series:

$$Nd(III) > Sm(III) > Pb(II) > Y(III) > Cd(II) > U(VI) > Ni(II) > Zn(II)$$

This ranking is difficult to correlate with the physico-chemical properties of selected metals as reported in Table S3. External criteria (metal concentration, speciation of the metals, etc.) may interfere in the effective affinity of the sorbent for these metal ions.

4. Conclusions

The grafting of glycine onto magnetic chitosan allows the elaboration of microparticles with enhanced sorption properties for heavy metal removal from aqueous solutions. Optimum sorption occurs around pH 5.5 through amine groups with the contribution of carboxylate moieties. The incorporation of magnetic nanoparticles facilitates ready

solid/liquid separation after the sorption and desorption steps. The small size makes it possible to reach equilibrium within 60 min of contact; however, the contribution of resistance to intraparticle diffusion to kinetic control cannot be neglected. Kinetic profiles are finely fitted by the PFORE. The maximum sorption capacities range between 0.33 mmol Hg g^{-1} and 0.46 mmol Ni or Zn g^{-1}. Globally, the sorption isotherms can be modeled using the Langmuir equation. In multi-metal solutions, the selectivity of the sorbent for target metal ions follows the trend: Hg(II)>>Pb(II)>>Cu(II)>>Ni(II)>>Zn(II)>>Cd(II). Acidic urea solution allows desorption of sorbed metal ions, and the sorbent can be recycled, maintaining high levels of sorption at the third cycle: the loss in sorption performance did not exceed ~9%. The sorbent was finally tested for the treatment of acidic leachates from Egyptian tailing ore (after pH control to 5.5). The occurrence of partial precipitation (Al(III), Cu(II) and Fe(III)) makes the interpretation of sorption performance more complex. The sorbent recovered a wide panel of metal ions, with preference for Zn(II), Ni(II) and Y(III) (in relation to their high relative concentrations in the feed solution). The sorbent is poorly selective and sorbs many of the metals present in the treated leachate. The precipitation phenomena and the effects of metal speciation and different metal concentrations in the complex effluent make difficult the correlation of selectivity with the physicochemical properties of metal ions and functional groups on the sorbent.

Supplementary Materials: The following are available online at https://www.mdpi.com/article/10.3390/app11188377/s1, Table S1a: Reminder on equations used for modeling uptake kinetics; Table S1b: Reminder on equations used for modeling sorption isotherms; Table S2: Composition of the ore sample collected on the Abu Thor site; Table S3a: FTIR assignments for glycine; Table S3b: FTIR assignments for chitosan; Table S3c: FTIR assignments for MCh; Table S3d: FTIR assignments for MChs and MChs*; Table S3e: FTIR assignments for G@MChs; Table S4: Physico-chemical properties of selected metals; Table S5: Composition of ore leachates.; Figure S1: Comparison of FTIR spectrum of pristine G@MChs with the spectrum of the sorbent after metal desorption; Figure S2: Determination of pH_{PZC}; Figure S3: Speciation diagrams for Ni(II), Zn(II), and Hg(II); Figure S4: pH variation during the sorption of Ni(II), Zn(II), and Hg(II) using G@MChs; Figure S5: Effect of sorbent dose on the sorption of Ni(II), Zn(II) and Hg(II) using G@MChs; Figure S6: Uptake kinetics for Ni(II), Zn(II) and Hg(II) using G@MChs—Modeling with the PSORE; Figure S7: Uptake kinetics for Ni(II), Zn(II) and Hg(II) using G@MChs—Modeling with the RIDE; Figure S8: Uptake kinetics for Ni(II), Zn(II) and Hg(II) using G@MChs from multi-component solutions—Modeling with the PSORE; Figure S9: Uptake kinetics for Ni(II), Zn(II) and Hg(II) using G@MChs from multi-component solutions—Modeling with the RIDE; Figure S10: Sorption isotherms for Ni(II), Zn(II) and Hg(II) using G@MChs for single-component solutions—Modeling with the Sips equation; Figure S11: SEM micrographs of sorbent before and after sorption of Ni(II), Zn(II) and Hg(II); Figure S12: Effect of temperature on the sorption of Ni(II), Zn(II) and Hg(II) using G@MChs at different initial metal concentrations; Figure S13: Metal sorption onto G@MChs from multi-component solutions; Figure S14: Selectivity coefficient ($SC_{Metal/Cadmium}$) (effect of increasing initial concentration); Figure S15: Treatment of ore leachate—(a) sorption capacities and (b) selectivity coefficients.

Author Contributions: Conceptualization, A.B., A.M. and E.G.; methodology, A.B. and M.F.H.; software, A.B. and E.G.; validation, K.Z.E., M.F.H. and E.G.; formal analysis, A.M. and M.F.H.; investigation, A.B. and E.G.; resources, K.Z.E. and M.F.H.; data curation, A.B., A.M. and E.G.; writing—original draft preparation, E.G.; writing—review and editing; K.Z.E., M.F.H. and E.G.; visualization, E.G.; supervision, E.G.; project administration, E.G.; funding acquisition, E.G. All authors have read and agreed to the published version of the manuscript.

Funding: This research received no external funding.

Institutional Review Board Statement: Not applicable.

Informed Consent Statement: Not applicable.

Data Availability Statement: Data available from authors.

Conflicts of Interest: The authors declare no conflict of interest.

References

1. Stefaniak, J.; Karwacka, S.; Janiszewska, M.; Dutta, A.; Rene, E.R.; Regel-Rosocka, M. Co(II) and Ni(II) transport from model and real sulfate solutions by extraction with bis(2,4,4-trimethylpentyl)phosphinic acid (Cyanex 272). *Chemosphere* **2020**, *254*, 126869. [CrossRef]
2. Diabate, P.D.; Boudesocque, S.; Mohamadou, A.; Dupont, L. Separation of cobalt, nickel and copper with task-specific amido functionalized glycine-betaine-based ionic liquids. *Sep. Purif. Technol.* **2020**, *244*, 116782. [CrossRef]
3. Daminova, S.S.; Kadirova, Z.C.; Sharipov, K.T.; Stoyko, O.V.; Chepulsky, S.A.; Adewuyi, A.; Hojamberdiev, M. Diisopropyldithiophosphoric acid-impregnated macroporous non-ionogenic styrene-divinylbenzene polymeric sorbent (Porolas) for effective copper extraction. *J. Ind. Eng. Chem.* **2017**, *55*, 204–214. [CrossRef]
4. Gupta, B.; Ismail, Z.B. Stabilization of solvent-impregnated resins (SIRs) by coating with water-soluble polymer and chemical cross-linking and its application in mercury removal. *Compos. Interfaces* **2006**, *13*, 487–506. [CrossRef]
5. Kitabayashi, T.; Sana, T.; Kiyoyama, S.; Takei, T.; Yoshida, M.; Shiomori, K. Extraction properties of Nickel (II) with polymeric particles with interconnected spherical pores impregnating with LIX84-I. *Solvent Extra. Res. Dev.-Jpn.* **2013**, *20*, 137–147. [CrossRef]
6. Shao, G.L.; Xiao, J.F.; Tian, Z.H.; Huang, J.J.; Yuan, S.G. Preparation and characterization of polyphenylene sulfide-based chelating resin-functionalized 2-amino-1,3,4-thiadiazole for selective removal Hg(II) from aqueous solutions. *Polym. Adv. Technol.* **2018**, *29*, 1030–1038. [CrossRef]
7. Perez, I.D.; Correa, M.M.J.; Tenório, J.A.S.; Espinosa, D.C.R. Effect of the pH on the recovery of Al3+, Co2+, Cr3+, Cu2+, Fe3+, Mg2+, Mn2+, Ni2+ and Zn2+ by Purolite S950. In *Energy Technology 2018—Carbon Dioxide Management and Other Technologies, Phoenix, AZ, USA*; Sun, Z., Wang, C., Guillen, D.P., Neelameggham, N.R., Zhang, L., Howarter, J., Wang, T., Olivetti, E., Zhang, M., Verhulst, D., et al., Eds.; Springer International Publishing: Cham, Switzerland; pp. 385–393.
8. Sajjadi, S.A.; Mohammadzadeh, A.; Tran, H.N.; Anastopoulos, I.; Dotto, G.L.; Lopicic, Z.R.; Sivamani, S.; Rahmani-Sani, A.; Ivanets, A.; Hosseini-Bandegharaei, A. Efficient mercury removal from wastewater by pistachio wood wastes-derived activated carbon prepared by chemical activation using a novel activating agent. *J. Environ. Manag.* **2018**, *223*, 1001–1009. [CrossRef]
9. Gu, S.Y.; Hsieh, C.T.; Gandomi, Y.A.; Yang, Z.F.; Li, L.Y.; Fu, C.C.; Juang, R.S. Functionalization of activated carbons with magnetic Iron oxide nanoparticles for removal of copper ions from aqueous solution. *J. Mol. Liq.* **2019**, *277*, 499–505. [CrossRef]
10. Johari, K.; Saman, N.; Mat, H. A comparative evaluation of mercury(II) adsorption equilibrium and kinetics onto silica gel and sulfur-functionalised silica gels adsorbents. *Can. J. Chem. Eng.* **2014**, *92*, 1048–1058. [CrossRef]
11. Wei, J.-W.; Wang, J.-H.; Zhao, S.-S.; Geng, L.-L. Synthesis and copper(II) affinity performance of amidoxime functionalized mesoporous silica. *J. Inorg. Mater.* **2016**, *31*, 449–453.
12. Das, S.; Samanta, A.; Gangopadhyay, G.; Jana, S. Clay-based nanocomposites as recyclable adsorbent toward Hg(II) capture: Experimental and theoretical understanding. *ACS Omega* **2018**, *3*, 6283–6292. [CrossRef] [PubMed]
13. Behbahani, M.; Zarezade, V.; Veisi, A.; Omidi, F.; Bagheri, S. Modification of magnetized MCM-41 by pyridine groups for ultrasonic-assisted dispersive micro-solid-phase extraction of nickel ions. *Int. J. Environ. Sci. Technol.* **2019**, *16*, 6431–6440. [CrossRef]
14. Romera, E.; Gonzalez, F.; Ballester, A.; Blazquez, M.L.; Munoz, J.A. Biosorption with algae: A statistical review. *Crit. Rev. Biotechnol.* **2006**, *26*, 223–235. [CrossRef]
15. Lopicic, Z.R.; Milojkovic, J.V.; Sostaric, T.D.; Petrovic, M.S.; Mihajlovic, M.L.; Lacnjevac, C.M.; Stojanovic, M.D. Influence of pH value on Cu(II) biosorption by lignocellulose peach shell waste material. *Hem. Ind.* **2013**, *67*, 1007–1015. [CrossRef]
16. Lazar, M.M.; Dinu, I.A.; Silion, M.; Dragan, E.S.; Dinu, M.V. Could the porous chitosan-based composite materials have a chance to a "NEW LIFE" after Cu(II) ion binding? *Int. J. Biol. Macromol.* **2019**, *131*, 134–146. [CrossRef]
17. Lu, S.; Yang, F.; Tian, C.; Shi, P.; Liu, X.; Bao, Z.; Nie, J. Iop, Sorption properties of ion-imprinted seaweed-chitosan composite adsorbents for nickel ions. In Proceedings of the 2019 5th International Conference on Energy Materials and Environment Engineering, Kuala Lumpur, Malaysia, 12–14 April 2019; Volume 295. [CrossRef]
18. Anuar, S.N.I.S.; Othman, F.; Chay, T.C.; Nasir, N.A.H.A. Biosorption of mercury ion (Hg^{2+}) using live and dead cells of *Rhizopus oryzae* and *Aspergillus niger*: Characterization, kinetic and isotherm studies. *J. Pure Appl. Microbiol.* **2020**, *14*, 1749–1760. [CrossRef]
19. Chokradjaroen, C.; Niu, J.; Panomsuwan, G.; Saito, N. Insight on solution plasma in aqueous solution and their application in modification of chitin and chitosan. *Int. J. Mol. Sci.* **2021**, *22*, 4308. [CrossRef] [PubMed]
20. Ferreira, L.M.B.; dos Santos, A.M.; Boni, F.I.; dos Santos, K.C.; Robusti, L.M.G.; de Souza, M.P.C.; Ferreira, N.N.; Carvalho, S.G.; Cardoso, V.M.O.; Chorilli, M.; et al. Design of chitosan-based particle systems: A review of the physicochemical foundations for tailored properties. *Carbohydr. Polym.* **2020**, *250*, 116968. [CrossRef]
21. Liu, X.-q.; Zhao, X.-x.; Liu, Y.; Zhang, T.-a. Review on preparation and adsorption properties of chitosan and chitosan composites. *Polym. Bull.* **2021**, 1–33. [CrossRef]
22. Nasrollahzadeh, M.; Sajjadi, M.; Iravani, S.; Varma, R.S. Starch, cellulose, pectin, gum, alginate, chitin and chitosan derived (nano) materials for sustainable water treatment: A review. *Carbohydr. Polym.* **2021**, *251*, 116986. [CrossRef]
23. Saheed, I.O.; Oh, W.D.; Suah, F.B.M. Chitosan modifications for adsorption of pollutants-A review. *J. Hazard. Mater.* **2021**, *408*, 124889. [CrossRef] [PubMed]
24. Sheth, Y.; Dharaskar, S.; Khalid, M.; Sonawane, S. An environment friendly approach for heavy metal removal from industrial wastewater using chitosan based biosorbent: A review. *Sustain. Energy Technol. Assess.* **2021**, *43*, 100951.
25. Guibal, E. Interactions of metal ions with chitosan-based sorbents: A review. *Sep. Purif. Technol.* **2004**, *38*, 43–74. [CrossRef]
26. Ko, E.; Kim, H. Preparation of chitosan aerogel crosslinked in chemical and ionical ways by non-acid condition for wound dressing. *Int. J. Biol. Macromol.* **2020**, *164*, 2177–2185. [CrossRef] [PubMed]

27. Takeshita, S.; Sadeghpour, A.; Sivaraman, D.; Zhao, S.; Malfait, W.J. Solvents, CO_2 and biopolymers: Structure formation in chitosan aerogel. *Carbohydr. Polym.* **2020**, *247*, 116680. [CrossRef] [PubMed]
28. Zhang, J.; Wang, Y.; Liang, D.; Xiao, Z.; Xie, Y.; Li, J. Sulfhydryl-modified chitosan aerogel for the adsorption of heavy metal ions and organic dyes. *Ind. Eng. Chem. Res.* **2020**, *59*, 14531–14536. [CrossRef]
29. Sahbaz, D.A.; Yakar, A.; Gunduz, U. Magnetic Fe_3O_4-chitosan micro- and nanoparticles for wastewater treatment. *Part. Sci. Technol.* **2019**, *37*, 728–736.
30. Zhang, L.; Xiong, Z.; Zhang, L.; Yu, B.; Zhang, W. Magnetic nanoparticles coated with dithizone-modified chitosan for use in solid-phase extraction of copper(II). *Anal. Methods* **2015**, *7*, 2050–2054. [CrossRef]
31. Kharissova, O.V.; Dias, H.V.R.; Kharisov, B.I. Magnetic adsorbents based on micro- and nano-structured materials. *RSC Adv.* **2015**, *5*, 6695–6719. [CrossRef]
32. Oshita, K.; Takayanagi, T.; Oshima, M.; Motomizu, S. Adsorption behavior of cationic and anionic species on chitosan resins possessing amino acid moieties. *Anal. Sci.* **2007**, *23*, 1431–1434. [CrossRef]
33. Hamza, M.F.; Aly, M.M.; Abdel-Rahman, A.A.H.; Ramadan, S.; Raslan, H.; Wang, S.; Vincent, T.; Guibal, E. Functionalization of magnetic chitosan particles for the sorption of U(VI), Cu(II) and Zn(II)—Hydrazide derivative of glycine-grafted chitosan. *Materials* **2017**, *10*, 539. [CrossRef] [PubMed]
34. Galhoum, A.A.; Hassan, K.M.; Desouky, O.A.; Masoud, A.M.; Akashi, T.; Sakai, Y.; Guibal, E. Aspartic acid grafting on cellulose and chitosan for enhanced Nd(III) sorption. *React. Funct. Polym.* **2017**, *113*, 13–22. [CrossRef]
35. Maia, M.T.; Sena, D.N.; Calais, G.B.; Luna, F.M.T.; Beppu, M.M.; Vieira, R.S. Effects of histidine modification of chitosan microparticles on metal ion adsorption. *React. Funct. Polym.* **2020**, *154*, 104694. [CrossRef]
36. Rafiee, F.; Karder, F.R. Bio-crosslinking of chitosan with oxidized starch, its functionalization with amino acid and magnetization: As a green magnetic support for silver immobilization and its catalytic activity investigation. *Int. J. Biol. Macromol.* **2020**, *146*, 1124–1132. [CrossRef]
37. WHO. *Guidelines for Drinking-Water Quality*, 4th ed.; WHO: Geneva, Switzerland, 2017.
38. Namdeo, M.; Bajpai, S.K. Chitosan-magnetite nanocomposites (CMNs) as magnetic carrier particles for removal of Fe(III) from aqueous solutions. *Colloids Surf. A* **2008**, *320*, 161–168. [CrossRef]
39. Donia, A.M.; Atia, A.A.; Abouzayed, F.I. Preparation and characterization of nano-magnetic cellulose with fast kinetic properties towards the adsorption of some metal ions. *Chem. Eng. J.* **2012**, *191*, 22–30. [CrossRef]
40. Lopez-Ramon, M.V.; Stoeckli, F.; Moreno-Castilla, C.; Carrasco-Marin, F. On the characterization of acidic and basic surface sites on carbons by various techniques. *Carbon* **1999**, *37*, 1215–1221. [CrossRef]
41. Galhoum, A.A.; Mahfouz, M.G.; Atia, A.A.; Abdel-Rehem, S.T.; Gomaa, N.A.; Vincent, T.; Guibal, E. Amino acid functionalized chitosan magnetic nanobased particles for uranyl sorption. *Ind. Eng. Chem. Res.* **2015**, *54*, 12374–12385. [CrossRef]
42. Shapiro, L. *Rapid Analysis of Silicate, Carbonate, and Phosphate Rocks*; Report Number 1401; US Government Printing Office: Washington, DC, USA, 1975; Volume 76, p. 88.
43. Marczenko, Z.; Balcerzak, M. Chapter 39—Rare-Earth Elements. In *Analytical Spectroscopy Library*; Location, Z., Balcerzak, M., Eds.; Elsevier: Amsterdam, The Netherlands, 2000; Volume 10, pp. 341–349.
44. Davies, W.; Gray, W. A rapid and specific titrimetric method for the precise determination of uranium using iron(II) sulphate as reductant. *Talanta* **1964**, *11*, 1203–1211. [CrossRef]
45. Bindu, V.U.; Mohanan, P.V. Thermal deactivation of alpha-amylase immobilized magnetic chitosan and its modified forms: A kinetic and thermodynamic study. *Carbohydr. Res.* **2020**, *498*, 108185. [CrossRef]
46. Laus, R.; Costa, T.G.; Szpoganicz, B.; Favere, V.T. Adsorption and desorption of Cu(II), Cd(II) and Pb(II) ions using chitosan crosslinked with epichlorohydrin-triphosphate as the adsorbent. *J. Hazard. Mater.* **2010**, *183*, 233–241. [CrossRef] [PubMed]
47. Coates, J. Interpretation of Infrared Spectra, A Practical Approach. In *Encyclopedia of Analytical Chemistry*; John Wiley & Sons, Ltd.: Hoboken, NJ, USA, 2006; pp. 1–23.
48. Pearson, R.G. Acids and bases. *Science* **1966**, *151*, 172–177. [CrossRef] [PubMed]
49. Sorlier, P.; Denuzière, A.; Viton, C.; Domard, A. Relation between the degree of acetylation and the electrostatic properties of chitin and chitosan. *Biomacromolecules* **2001**, *2*, 765–772. [CrossRef] [PubMed]
50. Williams, R. pKa Data (Compiled by R. Williams). Available online: http://www.chem.wisc.edu/areas/reich/pkatable/\protect\unhbox\voidb@x\hbox{pKa_compilation-1-Williams.pdf} (accessed on 4 June 2017).
51. Gustafsson, J.P. *Visual MINTEQ*, version 3.1; KTH, Royal Institute of Technology: Stockholm, Sweden, 2013.
52. Simonin, J.-P. On the comparison of pseudo-first order and pseudo-second order rate laws in the modeling of adsorption kinetics. *Chem. Eng. J.* **2016**, *300*, 254–263. [CrossRef]
53. Hubbe, M.A.; Azizian, S.; Douven, S. Implications of apparent pseudo-second-order adsorption kinetics onto cellulosic materials: A review. *BioResources* **2019**, *14*, 7582–7626. [CrossRef]
54. Rani, P.; Johar, R.; Jassal, P.S. Adsorption of nickel (II) ions from wastewater using glutaraldehyde cross-linked magnetic chitosan beads: Isotherm, kinetics and thermodynamics. *Water Sci. Technol.* **2020**, *82*, 2193–2202. [CrossRef]
55. Shehzad, H.; Farooqi, Z.H.; Ahmed, E.; Sharif, A.; Din, M.I.; Arshad, M.; Nisar, J.; Zhou, L.; Yun, W.; Nawaz, I.; et al. Fabrication of a novel hybrid biocomposite based on amino-thiocarbamate derivative of alginate/carboxymethyl chitosan/TiO_2 for Ni(II) recovery. *Int. J. Biol. Macromol.* **2020**, *152*, 380–392. [CrossRef]

56. Hamza, M.F.; Wei, Y.; Mira, H.I.; Abdel-Rahman, A.A.H.; Guibal, E. Synthesis and adsorption characteristics of grafted hydrazinyl amine magnetite-chitosan for Ni(II) and Pb(II) recovery. *Chem. Eng. J.* **2019**, *362*, 310–324. [CrossRef]
57. Al-Abbad, E.; Alakhras, F.; Anastopoulos, I.; Das, D.; Al-Arfaj, A.; Ouerfelli, N.; Hosseini-Bandegharaei, A. Chitosan-based materials for the removal of nickel ions from aqueous solutions. *Russ. J. Phys. Chem. A* **2020**, *94*, 748–755. [CrossRef]
58. Iordache, M.L.; Dodi, G.; Hritcu, D.; Draganescu, D.; Chiscan, O.; Popa, M.I. Magnetic chitosan grafted (alkyl acrylate) composite particles: Synthesis, characterization and evaluation as adsorbents. *Arabian J. Chem.* **2018**, *11*, 1032–1043. [CrossRef]
59. Tang, L.; Gou, S.; He, Y.; Liu, L.; Fang, S.; Duan, W.; Liu, T. An efficient chitosan-based adsorption material containing phosphoric acid and amidoxime groups for the enrichment of Cu(II) and Ni(II) from water. *J. Mol. Liq.* **2021**, *331*, 115815. [CrossRef]
60. Van Thuan, L.; My Uyen, D.; Hoang Sinh, L.; Dai Lam, T.; Van Dat, D.; Hoai Thuong, N. Adsorption of Ni(II) ions by magnetic activated carbon/chitosan beads prepared from spent coffee grounds, shrimp shells and green tea extract. *Environ. Technol.* **2020**, *41*, 2817–2832.
61. Bozorgi, M.; Abbasizadeh, S.; Samani, F.; Mousavi, S.E. Performance of synthesized cast and electrospun PVA/chitosan/ZnO-NH_2 nano-adsorbents in single and simultaneous adsorption of cadmium and nickel ions from wastewater. *Environ. Sci. Pollut. Res.* **2018**, *25*, 17457–17472. [CrossRef] [PubMed]
62. Igberase, E.; Ofomaja, A.; Osifo, P.O. Enhanced heavy metal ions adsorption by 4-aminobenzoic acid grafted on chitosan/epichlorohydrin composite: Kinetics, isotherms, thermodynamics and desorption studies. *Int. J. Biol. Macromol.* **2019**, *123*, 664–676. [CrossRef]
63. Abdelrahman, E.A.; Hegazey, R.M. Exploitation of Egyptian insecticide cans in the fabrication of Si/Fe nanostructures and their chitosan polymer composites for the removal of Ni(II), Cu(II), and Zn(II) ions from aqueous solutions. *Compos. Part B* **2019**, *166*, 382–400. [CrossRef]
64. Panahandeh, A.; Parvareh, A.; Moraveji, M. Synthesis and characterization of g-MnO_2/chitosan/Fe_3O_4 cross-linked with EDTA and the study of its efficiency for the elimination of zinc(II) and lead(II) from wastewater. *Environ. Sci. Pollut. Res.* **2020**, *28*, 9235–9254. [CrossRef]
65. Dev, V.V.; Baburaj, G.; Antony, S.; Arun, V.; Krishnan, K.A. Zwitterion-chitosan bed for the simultaneous immobilization of Zn(II), Cd(II), Pb(II) and Cu(II) from multi-metal aqueous systems. *J. Clean. Prod.* **2020**, *255*, 120309. [CrossRef]
66. Atangana, E. Adsorption of Zn(II) and Pb(II) ions from aqueous solution using chitosan cross-linked formaldehyde adsorbent to protect the environment. *J. Polym. Environ.* **2019**, *27*, 2281–2291. [CrossRef]
67. Shao, Z.; Lu, J.; Ding, J.; Fan, F.; Sun, X.; Li, P.; Fang, Y.; Hu, Q. Novel green chitosan-pectin gel beads for the removal of Cu(II), Cd(II), Hg(II) and Pb(II) from aqueous solution. *Int. J. Biol. Macromol.* **2021**, *176*, 217–225. [CrossRef]
68. Fu, Y.; Sun, Y.; Zheng, Y.; Jiang, J.; Yang, C.; Wang, J.; Hu, J. New network polymer functionalized magnetic-mesoporous nanoparticle for rapid adsorption of Hg(II) and sequential efficient reutilization as a catalyst. *Sep. Purif. Technol.* **2021**, *259*, 118112. [CrossRef]
69. Usman, M.; Ahmed, A.; Yu, B.; Wang, S.; Shen, Y.; Cong, H. Simultaneous adsorption of heavy metals and organic dyes by β-cyclodextrin-chitosan based cross-linked adsorbent. *Carbohydr. Polym.* **2021**, *255*, 117486. [CrossRef] [PubMed]
70. Abdelrahman, E.A.; Subaihi, A. Application of geopolymers modified with chitosan as novel composites for efficient removal of Hg(II), Cd(II), and Pb(II) ions from aqueous media. *J. Inorg. Organomet. Polym Mater.* **2020**, *30*, 2440–2463. [CrossRef]
71. Hamza, M.F.; Wei, Y.; Benettayeb, A.; Wang, X.; Guibal, E. Efficient removal of uranium, cadmium and mercury from aqueous solutions using grafted hydrazide-micro-magnetite chitosan derivative. *J. Mater. Sci.* **2020**, *55*, 4193–4212. [CrossRef]
72. Zhang, D.; Wang, L.; Zeng, H.; Rhimi, B.; Wang, C. Novel polyethyleneimine functionalized chitosan-lignin composite sponge with nanowall-network structures for fast and efficient removal of Hg(II) ions from aqueous solution. *Environ. Sci. Nano* **2020**, *7*, 793–802. [CrossRef]
73. Zeng, H.; Wang, L.; Zhang, D.; Wang, F.; Sharma, V.K.; Wang, C. Amido-functionalized carboxymethyl chitosan/montmorillonite composite for highly efficient and cost-effective mercury removal from aqueous solution. *J. Colloid Interface Sci.* **2019**, *554*, 479–487. [CrossRef]
74. Saha, G.C.; Hoque, M.I.U.; Miah, M.A.M.; Holze, R.; Chowdhury, D.A.; Khandaker, S.; Chowdhury, S. Biosorptive removal of lead from aqueous solutions onto Taro (*Colocasia esculenta* (L.) Schott) as a low cost bioadsorbent: Characterization, equilibria, kinetics and biosorption-mechanism studies. *J. Environ. Chem. Eng.* **2017**, *5*, 2151–2162. [CrossRef]
75. Lima, E.C.; Hosseini-Bandegharaei, A.; Moreno-Piraján, J.C.; Anastopoulos, I. A critical review of the estimation of the thermodynamic parameters on adsorption equilibria. Wrong use of equilibrium constant in the Van't Hoof equation for calculation of thermodynamic parameters of adsorption. *J. Mol. Liq.* **2019**, *273*, 425–434. [CrossRef]